


## Interface Engineering of Electrical Contacts

Sneha Banerjee<sup>1</sup>,<sup>1</sup> John Luginsland<sup>2</sup>,<sup>2</sup> and Peng Zhang<sup>1,\*</sup>

<sup>1</sup>*Department of Electrical and Computer Engineering, Michigan State University, East Lansing, Michigan 48824-1226, USA*

<sup>2</sup>*Confluent Sciences, LLC, Albuquerque, New Mexico 87111, USA*

 (Received 9 April 2021; revised 1 June 2021; accepted 2 June 2021; published 21 June 2021)

Highly conductive nanoscale electrical contacts suffer from strong current crowding at the contact edges, which can lead to nonuniform heat deposition; the formation of local hot spots, aggravation of electromigration; and, in the worst-case scenario, lead to thermal runaway and breakdown of the device. These effects severely affect the overall device properties, reliability, and lifetime. Devices based on thin-film junctions, nanotubes or nanowires, and two-dimensional (2D) materials are especially sensitive to current transport at electrical contacts, due to their reduced dimensions and increased geometrical confinement for current flow. Here, we demonstrate a method to mitigate current crowding, by engineering the interface layer properties and geometry. Based on a self-consistent transmission-line model, we show that the distribution of the contact current greatly depends on the properties of the interfacial layer between two contacting members. Current steering and redistribution can be realized by strategically designing the specific contact resistivity,  $\rho_c$ , along the contact length. For similar contact members, parabolically varying  $\rho_c$  along the contact interface significantly reduces the edge-current crowding in ohmic contacts. Similarly, the nonuniform current distribution of 2D semiconductor-3D metal contacts can be decreased, and the current-transfer length can be increased by varying the Schottky barrier height along the interface. It is also found that introducing a nanometer- or subnanometer-scale thin insulating tunneling gap between contact members can greatly reduce current crowding, while maintaining a similar total contact resistance.

DOI: [10.1103/PhysRevApplied.15.064048](https://doi.org/10.1103/PhysRevApplied.15.064048)

### I. INTRODUCTION

Engineering electrical contacts to achieve desired interface current transport is crucial for next-generation electronics [1,2]. Current crowding and contact resistance are the two main limiting factors for the development of nanocircuits based on thin films, nanotubes or nanowires, and two-dimensional (2D) materials [3–9]. In particular, current crowding [4,10–17], where the distribution of the current density becomes highly inhomogeneous at the contact area, severely affects the device properties, reliability, and lifetime [8,18]. It leads to localized overheating, which may cause the formation of thermal hot spots [19–21], thermal runaway [22], and the acceleration of electromigration process [10,23–26]. In the long term, these effects may eventually result in failure of the chip. In recent times, these electrothermal effects have become one of the most critical concerns of very-large-scale integration (VLSI) circuit designers because of the growing demands for high switching speed and high packing density [27–32]. In miniaturized electronic circuits, current-crowding effects are more severe and cause greater on-chip power density [33], which makes power dissipation one of

the critical issues in the electronics industry today [34,35]. Current crowding is also responsible for  $1/f$  noise generation and third-harmonic distortion in semiconductor devices [36]. Devices based on low-dimensional nanostructures suffer from adverse effects of inhomogeneous current distribution at the contact area. Many experiments have provided clear evidence of current crowding in field-effect transistors based on 2D materials, such as black phosphorus [18],  $\text{MoS}_2$  [37], and graphene [38,39]. Current transport in 2D semiconductor-three-dimensional (3D) metal contacts is found to be concentrated at the front edge [8,18,37,40], which causes localized Joule heating, contact noise [38], and device malfunctioning and failure [18].

Several efforts have been made to reduce current crowding and improve current transport in electrical contacts by making the proper choice of electrode thickness [41], doping, material, and geometry [42–44]; optimizing the current-spreading layer [45]; and optimizing the gate-bias voltage [18]. State-of-the-art methods to overcome current crowding also include reducing the injection barrier at the contact interface with thin interlayers, or inserting additional control contacts to increase charge injection [46]. Existing studies give no indication of the variation of current along the contact length and the

\*[pz@egr.msu.edu](mailto:pz@egr.msu.edu)

importance of interface layer engineering to diminish current-crowding effects. Crowding is especially strong for contacts with low specific contact resistivity [13,14,47]. Increasing specific contact resistivity tends to reduce current crowding; however, it increases the total contact resistance that may lead to increased Joule heating and degradation of the contact. Because of this trade-off, it is particularly challenging to design electrical interfaces to reduce current crowding without decreasing the total current in the circuit or suffering unacceptably high voltages.

Our previous studies [12,14] showed that current and voltage distribution along the contact length greatly depended on the interfacial layer properties and geometry. Here, we demonstrate how to precisely customize their profiles along the contact length by interface engineering. We characterize ohmic, Schottky [40,48], and tunneling-type [14,49–51] electrical contacts. Our goal is to maximize control over electrical contact operation and heat distribution by strategically varying the specific contact resistivity,  $\rho_c$ , along the contact length. We use a modified two-dimensional transmission-line model (TLM) [12,14], where  $\rho_c$  depends upon the local voltage drop and contact-current density. The spatial variation of  $\rho_c$  may be achieved by varying the doping, thickness, or shape of the contact layer, or by introducing impurities, such as resistive contaminants, oxides, or foreign objects along the interface. The electrical properties of the engineered interfaces are investigated for various input voltages, contact dimensions and geometries, and material properties. Solving the TLM equations self-consistently, we find spatial profiles of  $\rho_c$  that can reduce current crowding, increase current-transfer length, improve current transport, and steer and redistribute current in the contact area. Most importantly, we find that severe current crowding in highly conductive ohmic contacts can be eliminated by introducing a thin tunneling layer between the contact members. If the tunneling layer is sufficiently thin and the contact length is large, the change in the total contact resistance is found to be insignificant.

The methods used here can be applied to characterize various contact geometries, as shown in Fig. 1. Controlled current and voltage distribution can be achieved via engineered spatially varying contact layer properties and geometry (Fig. 1) [2]. Notably, the transmission-line model, in general, underestimates the extent of current crowding, which may be more accurately accounted for by field-solution approaches [13,16,47]. However, such simplified models have been used successfully to capture the basic scaling and physics for the characterization of mesoscale and nanoscale electrical contacts [11, 12,14,15,52,53]. Here, we analyze nanoscale copper (Cu) thin-film contacts and gold-MoS<sub>2</sub> contacts as examples. The concepts, approaches, and results should be important to the design of any circuits where electrical contacts are of concern, such as semiconductor devices [15,54], integrated circuits [55], low-dimensional-material-based electronics [1,5,37,56], nanoscale devices [57–61], cathodes and emitters [30,62–67], and all-solid-state batteries [68].

## II. THE MODEL

The formulation is based on a modified TLM for Cartesian [14] and circular [12] contact structures, coupled with an improved thermionic emission current-injection model for 2D materials [40,48] (for 2D/3D Schottky contacts), or the self-consistent quantum model for one-dimensional metal-insulator-metal (*M-I-M*) junctions [51,69] (for tunneling-type contacts). Notably, the TLM here is not related to the transmission-line measurement or transfer-length measurement (also abbreviated as “TLM”) used to determine the contact resistance in transistors [15]. As shown in Fig. 2, the sheet resistances of the two contacting members are  $R_{sh1}$  and  $R_{sh2}$ , respectively. The spatially dependent specific interfacial resistivities (also termed specific contact resistivities) are  $\rho_c(x)$  and  $\rho_c(r)$  for the Cartesian and circular contacts, respectively. The goal is to engineer a spatial profile of  $\rho_c(x)$  or  $\rho_c(r)$  to suppress current crowding. While the modified TLMs have

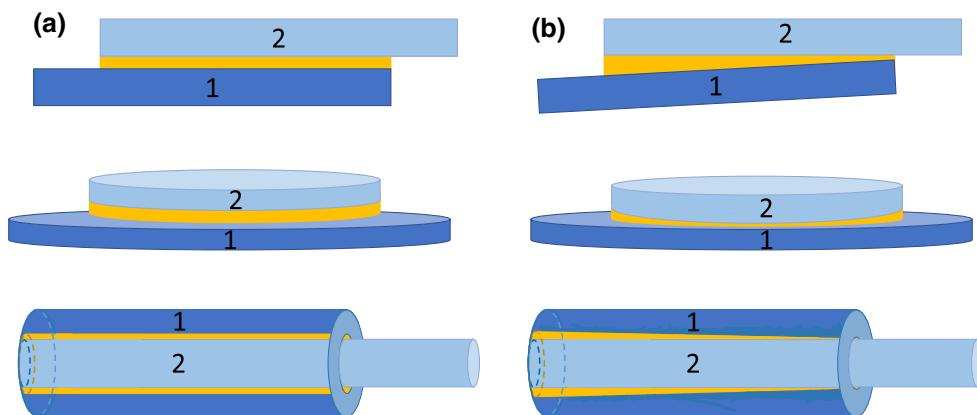


FIG. 1. Electrical contact between contact members 1 and 2 for different electrode geometries. (a) Electrical contact with uniform contact interface; (b) electrical contact with spatially varying engineered interfacial layer, which is used to control voltage and current distribution.

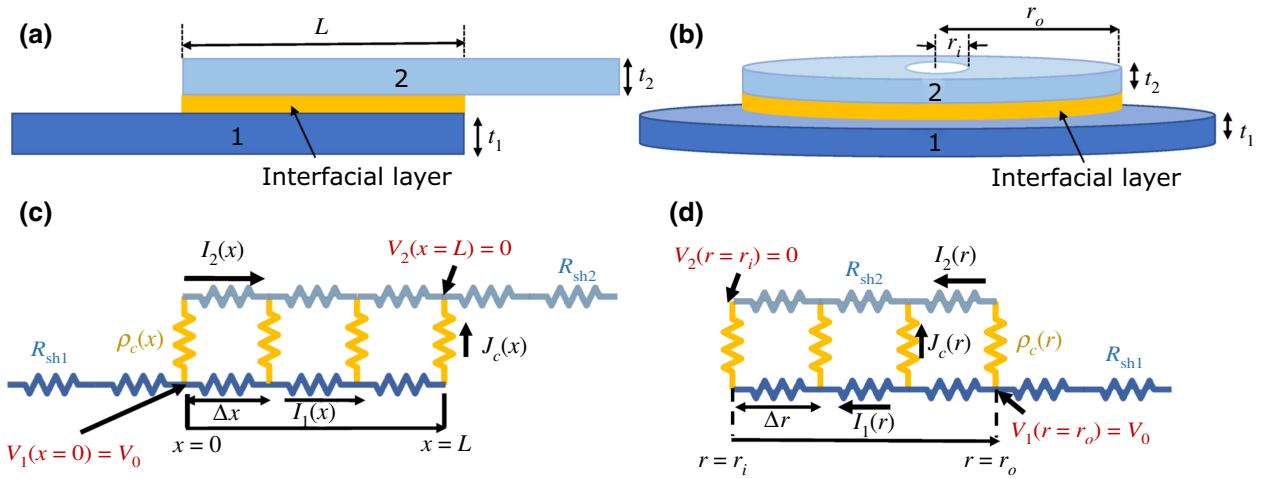


FIG. 2. Electrical contact between two contacting members in (a) Cartesian, (b) circular geometry. (c)(d) Corresponding transmission-line models. In (a),(b), thin interface layer (ohmic, Schottky, or tunneling type) is sandwiched between two contacting members. Thicknesses of thin films 1 and 2 are  $t_1$  and  $t_2$ , respectively.

been presented before [12,14], the governing equations are given below for completeness.

For the Cartesian electrical contacts in Fig. 2(a), the TLM in Fig. 2(c) gives [14]

$$\begin{aligned} \frac{\partial I_1(x)}{\partial x} &= -wJ_c(x), & \frac{\partial V_1(x)}{\partial x} &= -\frac{I_1(x)R_{sh1}}{w}, \\ \frac{\partial I_2(x)}{\partial x} &= wJ_c(x), & \frac{\partial V_2(x)}{\partial x} &= -\frac{I_2(x)R_{sh2}}{w}, \end{aligned} \quad (1)$$

where  $I_{1,2}(x)$  represents the current flowing at  $x$  through the lower or upper contact member, respectively;  $V_{1,2}(x)$  is the local voltage at  $x$  along the lower or upper contact member, respectively;  $w$  is the effective transverse dimension of the contacts; and  $J_c(x) = V_g(x)/\rho_c(x)$  and  $V_g(x) = V_1(x) - V_2(x)$  are the local current density and local voltage drop across the contact interface at  $x$ , respectively. Notably, from Eq. (1),  $I_1(x) + I_2(x) = I_{tot} = \text{constant}$ , where  $I_{tot}$  is the total current in the circuit, to be determined from the boundary conditions,

$$\begin{aligned} V_1(x=0) &= V_0, & I_2(x=0) &= 0, \\ I_1(x=L) &= 0, & V_2(x=L) &= 0, \end{aligned} \quad (2)$$

where we assume the voltage of the upper contact member at  $x = L$  is zero, and the externally applied voltage at  $x = 0$  of the lower contact member is  $V_0$ . Notably,  $I_1(x=0) = I_{tot}$  and  $I_2(x=0) = 0$ . For the contact model in Fig. 2(c), the contact resistance is defined as

$$R_c = \frac{V_1(0) - V_2(L)}{I_{tot}} = \frac{V_0}{I_{tot}}. \quad (3)$$

For circular (ring) electrical contacts shown in Fig. 2(b) with the TLM in Fig. 2(d), we have [12]

$$\begin{aligned} \frac{\partial I_1(r)}{\partial r} &= 2\pi r J_c(r), & \frac{\partial V_1(r)}{\partial r} &= \frac{I_1(r)R_{sh1}}{2\pi r}, \\ \frac{\partial I_2(r)}{\partial r} &= -2\pi r J_c(r), & \frac{\partial V_2(r)}{\partial r} &= \frac{I_2(r)R_{sh2}}{2\pi r} \end{aligned} \quad (4)$$

where  $I_{1,2}(r)$  represents the current flowing at  $r$  along the radial direction of thin films 1 and 2, respectively, and  $V_{1,2}(r)$  is the local voltage at  $r$  along the radial direction of thin films 1 and 2, respectively.  $J_c(r) = V_g(r)/\rho_c(r)$  and  $V_g(r) = V_1(r) - V_2(r)$  are the local current density and the local voltage drop across the contact interface at  $r$ , respectively. From Eq. (4),  $I_1(r) + I_2(r) = I_{tot} = \text{constant}$ , where  $I_{tot}$  is the total current in the circuit to be determined from the following boundary conditions:

$$\begin{aligned} V_1(r=r_o) &= V_0, & I_1(r=r_i) &= 0, \\ I_2(r=r_o) &= 0, & V_2(r=r_i) &= 0, \end{aligned} \quad (5)$$

where we assume the voltage of the upper contact member at  $r = r_i$  is zero and the external voltage  $V_0$  is applied at  $r = r_o$  to the lower contact member;  $r_o$  is the outer radius of thin film 2 and  $r_i$  is the inner radius of both films. Notably,  $I_1(r=r_o) = I_{tot}$ ,  $I_2(r=r_i) = I_{tot}$ , and  $I_{tot} = \int_{r_i}^{r_o} 2\pi r J_c(r) dr$ . For the contact model in Fig. 2(d), the contact resistance is defined as

$$R_c = \frac{V_1(r_o) - V_2(r_i)}{I_{tot}} = \frac{V_0}{I_{tot}}. \quad (6)$$

For ohmic contacts,  $\rho_c(x)$  and  $\rho_c(r)$  can be prescribed. For 2D semiconductor-3D metal Schottky contacts, the local contact-current density,  $J_c(x)$  or  $J_c(r)$ , is calculated

from the 2D thermionic emission model [40,48], and for  $M$ - $I$ - $M$  tunneling-type contacts, it is calculated from the one-dimensional  $M$ - $I$ - $M$  quantum-tunneling model including space-charge effects [51,69].  $\rho_c(x)$  and  $\rho_c(r)$  are then determined from these contact-current densities by  $\rho_c = V_g/J_c$ . The coupled equations are solved self-consistently. More detailed descriptions are given in Refs. [12,14].

We first characterize both Cartesian and circular ohmic contacts with varying  $\rho_c$  along the contact length or radius, respectively. We find varying  $\rho_c(x)$  parabolically and  $\rho_c(r)$  linearly can effectively reduce the current-crowding effects in planar and circular ohmic contacts, respectively. Next, we analyze the 2D semiconductor-3D metal contacts to increase the current-transfer length by varying the Schottky barrier height (SBH) along contact length  $L$ . Finally, we introduce a thin tunneling layer between the highly conductive contact members to reduce current crowding, without increasing the total contact resistance significantly.

### III. RESULTS AND DISCUSSION

We analyze Cartesian ohmic contacts in Fig. 3 and circular ohmic contacts in Fig. 4. The input voltage  $V_0 = 0.6$  V is the required industry standard, according to the International Roadmap for Devices and Systems (IRDS) [70] for the year 2030, which is given to contact member 1, at  $x = 0$  for the planar structure and at  $r = r_o$  for the circular structure. Upper contact members at  $x = L$  [Figs. 2(a) and 2(c)] and  $r = r_i$  [Figs. 2(b) and 2(d)] are grounded for the two structures under study. The

thicknesses of both contact members are assumed to be the same:  $t_1 = t_2 = 10$  nm. The spatial or radial variation of  $\rho_c$  can be realized by varying the doping, thickness, or geometry of the contact layer, or by introducing impurities, such as resistive contaminants, oxides, or foreign objects along the interface [14,72–76]. In Fig. 3, we explore the reduction of severe current crowding [c.f. Fig. 3(a), black dotted line] at the highly conductive planar (or Cartesian) Cu/Cu ohmic contacts by varying the interfacial layer resistivity parabolically along the contact length. For our calculations, we assume  $\rho_c(x) = 1.8 \times 10^{-9} \{B[(2x/L) - 1]^2 + 0.01\} \Omega \text{ cm}^2$  with the minimum at half of the contact length, where  $B$  is a constant. The sheet resistance of copper (Cu) is  $R_{\text{sh}} = 18 \Omega/\square$  [12,71], where the unit of sheet resistance,  $\Omega/\square$ , is “ohms per square” [13,15,52]. The contact length  $L$ , is 100 nm, and the width (transverse dimension),  $w$ , of the contact members is 10 nm. Figure 3(a) shows that the profile of contact-current density,  $J_c(x)$ , strongly depends on  $B$ . The profiles of  $J_c(x)$  can be explained by simple current-transport theory in a circuit, where electric current flows through the least-resistive path. When  $B$  is increased, the inhomogeneity of the contact-current distribution decreases. At around  $B = 0.2$ , the interfacial current becomes almost uniform along the contact length. The total contact resistance,  $R_c$ , as a function of  $B$  is plotted in Fig. 3(b) for different contact lengths. For all contact lengths plotted here,  $R_c$  increases only slightly with  $B$ , e.g., for  $L = 100$  nm,  $R_c$  is increased at most by 50% within the range of  $B$ . Hence, evidently, it is possible to eliminate current-crowding effects and achieve uniform contact-current distribution without

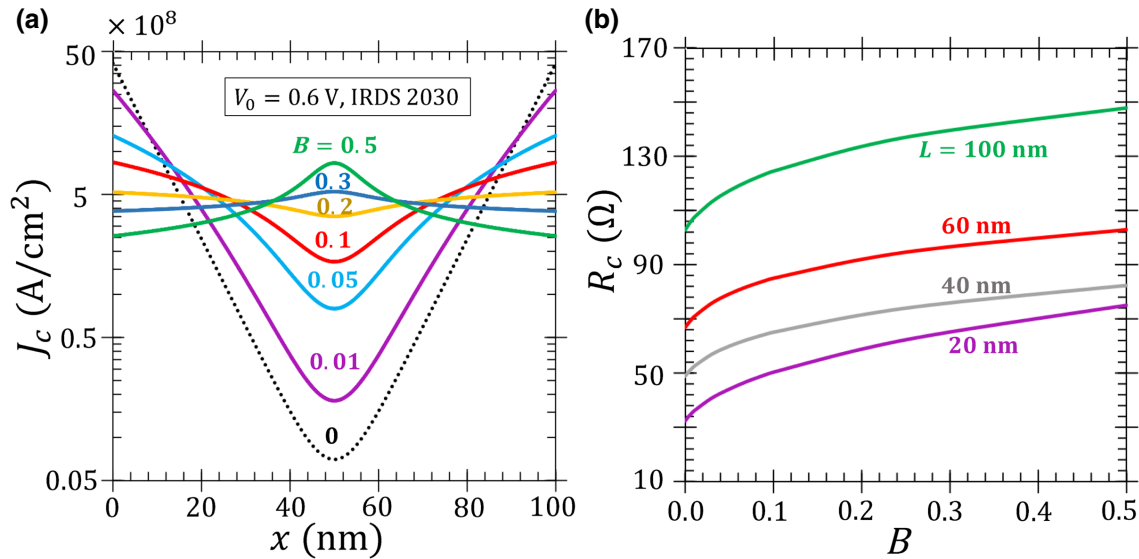


FIG. 3. Engineered ohmic contact in Cartesian geometry (Fig. 2a) with specific contact resistivity  $\rho_c(x) = 1.8 \times 10^{-9} \{B [(2x/L) - 1]^2 + 0.01\} \Omega \text{ cm}^2$ . (a) Contact-current density,  $J_c(x)$ , along contact length for different values of  $B$ ; (b) contact resistance as a function of  $B$  for different contact lengths  $L$ . Input voltage  $V_0 = 0.6$  V is the required industry standard, according to the IRDS [70] for the year 2030. Thicknesses of both Cu contact members are 10 nm, with a resistivity of  $18 \mu\Omega \text{ cm}$  [71], which gives sheet resistance  $R_{\text{sh}1} = R_{\text{sh}2} = 18 \Omega/\square$ . Contact length,  $L$ , is 100 nm, and width (transverse dimension),  $w$ , of the contact members is 10 nm.

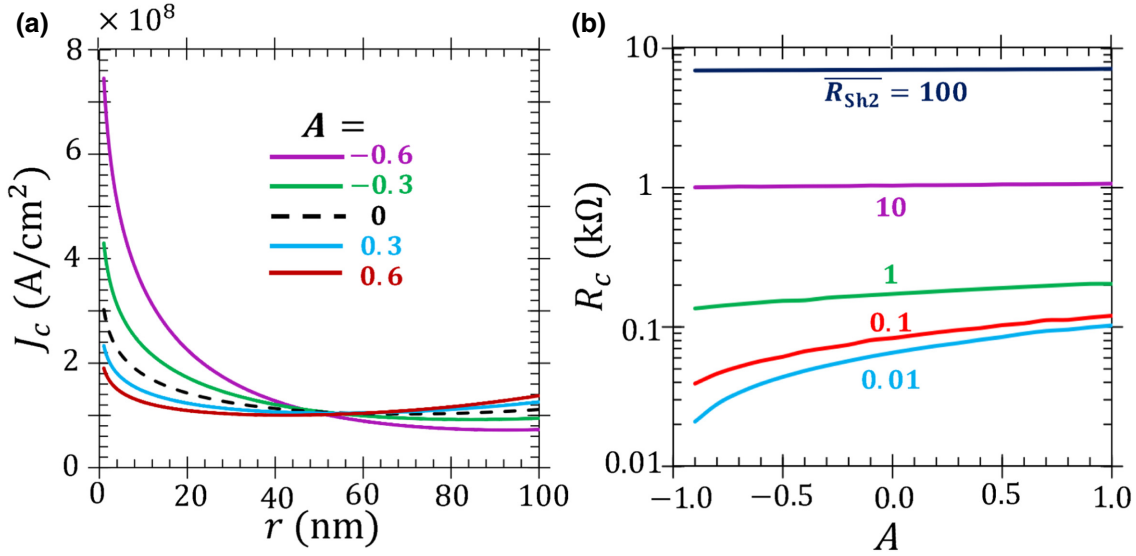


FIG. 4. Ohmic contacts in circular geometry [Fig. 2(b)] with linearly varying specific contact resistivity. (a) Contact-current density,  $J_c$ , along contact length for different values of linear constant  $A$ . (b) Contact resistance as a function of  $A$  for different sheet resistance ratios  $\overline{R}_{sh2}$ . Here, we use  $\rho_c(r) = 1.8 \times 10^{-9}(1 + Ar/r_o) \Omega \text{ cm}^2$ . In (a),  $\overline{R}_{sh2} = R_{sh2}/R_{sh1} = 1$ . Input voltage  $V_0 = 0.6 \text{ V}$  is the required industry standard, according to the IRDS [70] for the year 2030. Contact member 1 is assumed to be copper (Cu) with sheet resistance  $R_{sh1} = 18 \Omega/\square$  [12,71]; outer radius of upper contact member,  $r_o$ , is 100 nm, and inner radius of both contact members,  $r_i$ , is 1 nm.

sacrificing the total current in the circuit. In practical circuit design and fabrication, where it might be difficult to control the shape of a parabola, one can use a step variation by just making the edges of a contact interface (of planar similar contact members) more resistive than the rest of the contact area (see Appendix). The approach used here to minimize the current-crowding effects can be extended to contacts with different electrode thicknesses, materials, and geometries.

In Fig. 4, we investigate the current transport for circular ohmic contacts with linearly varying specific contact resistivity along the contact radius. Notably, linearly varying the specific contact resistivity is found to strongly modify the current density profile for planar contacts [14]. Here, we assume radially varying  $\rho_c(r) = 1.8 \times 10^{-9}(1 + Ar/r_o) \Omega \text{ cm}^2$ , an outer radius of the upper contact member [Fig. 2(b)],  $r_o$ , of 100 nm, and an inner radius of both contact members  $r_i$  of 1 nm.  $A$  is a linear constant. Contact member 1 is assumed to be copper (Cu) with a sheet resistance  $R_{sh1}$  of  $18 \Omega/\square$  [12,71].

As shown in Fig. 4(a), linear variation of  $\rho_c(r)$  can reduce the current-crowding effects for circular contacts. In particular, current crowding at the inner edge reduces significantly when  $A$  is positive. Figure 4(b) shows that for circular contacts  $R_c$  increases with  $A$  rapidly for  $\overline{R}_{sh2} < 1$  and remains almost constant when  $\overline{R}_{sh2} \gg \overline{R}_{sh1}$ . Therefore, one can get a desired interfacial current distribution profile without altering the overall contact resistance considerably. Hence, engineering the spatially varying interfacial contact resistivity can provide strategic thermal management of the integrated circuits and systems.

Current crowding is an unavoidable consequence of geometrical confinement and resistivity mismatch at the 2D semiconductor-3D metal Schottky junctions, where current transport between the semiconductor and the metal contact is concentrated at the front edge of the contact [8,18,36–40]. In Fig. 5, we study the engineering of such contacts by spatially varying the SBH. We use the one-dimensional (1D) thermionic emission equation for 2D materials [40,48], coupled with the TLM equations, Eqs. (1) and (2) [14], to analyze such 2D/3D contacts. For a 2D transition-metal dichalcogenide (TMDC), such as atomically thin MoS<sub>2</sub>, the thermionic emission is governed by

$$J_{th}(V_g, T) = \frac{2e\Phi_{B0}k_B T}{\pi \tau \hbar^2 v_F^2} \left(1 + \frac{k_B T}{\Phi_{B0}}\right) \exp\left(-\frac{\Phi_{B0} - \varepsilon_F}{k_B T}\right),$$

where  $\Phi_{B0} = \phi_B + \varepsilon_F$  is the intrinsic SBH,  $\varepsilon_F$  is the Fermi level,  $\phi_B$  is the SBH, the Fermi velocity ( $v_F$ ) is  $1.1 \times 10^6 \text{ m/s}$  for MoS<sub>2</sub>, and  $\tau \approx (0.1 - 10) \text{ ps}$  is the carrier injection time determined experimentally [78]. The local contact-current density at any position  $x$  along the contact length is

$$J_c(V_g, T) = J_{th}(V_g, T) \left[ \exp\left(\frac{eV_g}{k_B T}\right) - 1 \right].$$

We assume that the SBH is a function of  $x$ , so  $\phi_B(x) = 0.4(x/L)^2 - b(x/L) + 0.8 \text{ eV}$ , where  $b$  is a constant, as shown in Fig. 5(a). The injection-current density at the contact interface for different values of  $b$  is shown in



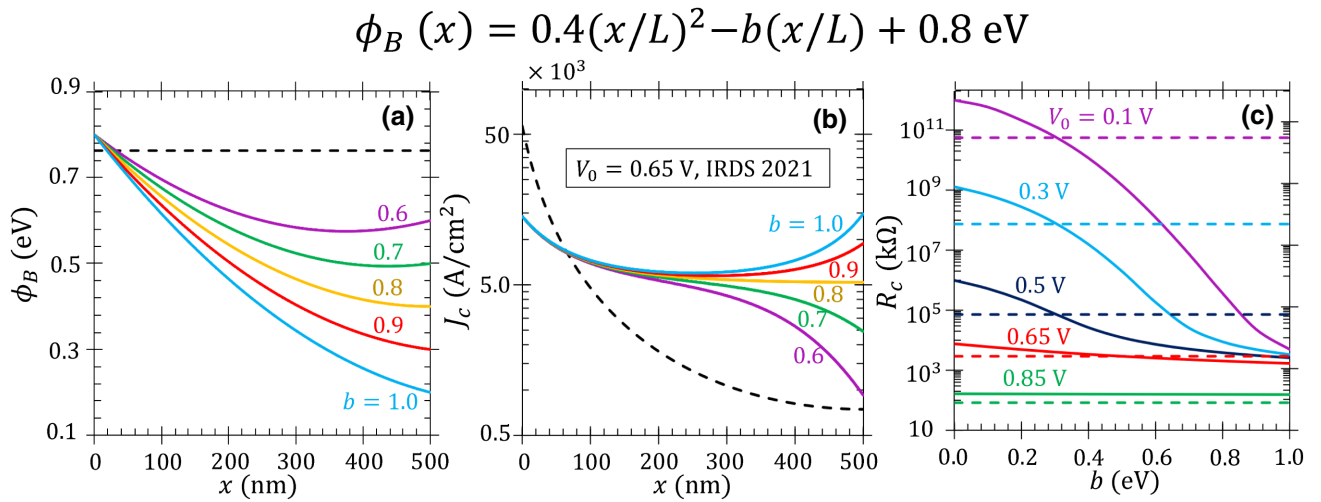


FIG. 5. Engineered Schottky contacts in Cartesian geometry. (a) Schottky barrier height  $\phi_B(x)$ , (b) corresponding contact-current density,  $J_c(x)$ , along contact length for MoS<sub>2</sub>/Au contacts for different values of  $b$ , and (c) contact resistance as a function of  $b$  for different input voltage  $V_0$ . Dashed lines are for MoS<sub>2</sub>/Au contacts with uniform  $\phi_B = 0.763$  eV [77].  $\varepsilon_F = 0.077$  eV [77] and  $\tau = 0.1$  ps. Bias voltage  $V_0 = 0.65$  in (b) is the required industry standard, according to the IRDS [70] for the year 2021. Here,  $R_{\text{sh1}}(\text{MoS}_2) = 59171.6 \Omega/\square$ ,  $R_{\text{sh2}}(\text{Au}) = 2.2 \Omega/\square$ ,  $L = 500$  nm, and  $T = 300$  K.

Fig. 5(b). Notably, one can also use a simpler function of  $\phi_B$  along  $x$  to mitigate current crowding (see Appendix). It is found that current crowding for a uniform SBH (cf. black dashed line in Fig. 5) can be reduced considerably by choosing the value of  $b$  [e.g., Fig. 5(b),  $b = 0.8$ ]. The bias voltage  $V_0 = 0.65$  V is the required industry standard, according to the IRDS [70] for the year 2021. Figure 5(c) shows the contact resistance as a function of  $b$  for different input voltages,  $V_0$ . Dashed lines are for MoS<sub>2</sub>/Au contacts with uniform  $\phi_B = 0.763$  eV along the contact [77]. We see that the total contact resistance depends strongly on parameter  $b$  and input voltage  $V_0$ . The difference in contact resistance for engineered and uniform SBHs is large for low bias voltages, but becomes smaller for high bias voltages, for the chosen specific case here. Since the thermionic charge injection current for 2D materials sensitively depends on both the bias voltage and temperature [40,48,79], the engineered SBH profile requires a more detailed characterization for practical implementation.

Next, we investigate the reduction of current crowding for highly conductive ( $\rho_c \sim 10^{-11} \Omega \text{ cm}^2$ ) ohmic contacts by tunneling engineering. We introduce a thin insulating layer of uniform thickness along the contact length between the contact members. Current transport in the contact region is no longer ohmic and is governed by the quantum-tunneling phenomenon [49–51,69]. We solve Eqs. (1) and (2) along with the  $M$ - $I$ - $M$  tunneling-junction equation [51,69]. The local contact-current density,  $J_c(x)$ , at any location  $x$  from contact member 1 to contact member 2 is calculated based on the coupled 1D Schrödinger-Poisson solutions in the  $M$ - $I$ - $M$  junction [51,69]. Our quantum model of the junction includes emissions from

both the cathode (contacting member 2) and the anode (contacting member 1), the effects of image charge potential [51], space charge, and exchange-correlation potentials [80]. For given values of the work function of the two contact members,  $W_{1,2}$ , electron affinity  $X$ , thickness  $D$ , and relative permittivity  $\varepsilon_r$  of the insulator layer, the local contact-current density  $J_c(x)$  can be calculated from this 1D quantum model for an input of the contact voltage drop,  $V_g(x)$ , at any location  $x$  [51,69]. The calculation of this  $J_c(x) - V_g(x)$  relation is coupled with the TLM, Eqs. (1) and (2), and is solved self-consistently.

We consider nanometer- and subnanometer-scale tunneling layers in Figs. 6 and 7, respectively. The current fabrication technology can manufacture nodes as small as 3 nm [81,82]. The IRDS [70] predicts that 1.0-nm nodes may be implemented tentatively within a few years, and the scale is expected to go down even further, to subnanometers. Noting the table in Fig. 6(a), we show our calculations for both “thin” insulating gaps at 1 nm, suitable for future deployment, and “thick” gaps at 3 nm, which would be suitable for near-term testing of this concept as a proof-of-principle experiment for advanced contacts.

Figure 6 shows the contact-current density  $J_c(x)$ , and the specific contact resistivity  $\rho_c(x)$  along the contact length for Cartesian contacts. For these calculations, the contact length is assumed to be 100 nm. The width and thickness of both contact members are 10 nm. Solid lines are for self-consistent numerical calculations for the tunneling-type contacts, using Eqs. (1) and (2), and  $M$ - $I$ - $M$  quantum-tunneling formulations [51,69], for different values of gap distance (insulator layer thickness)  $D$  and work function of

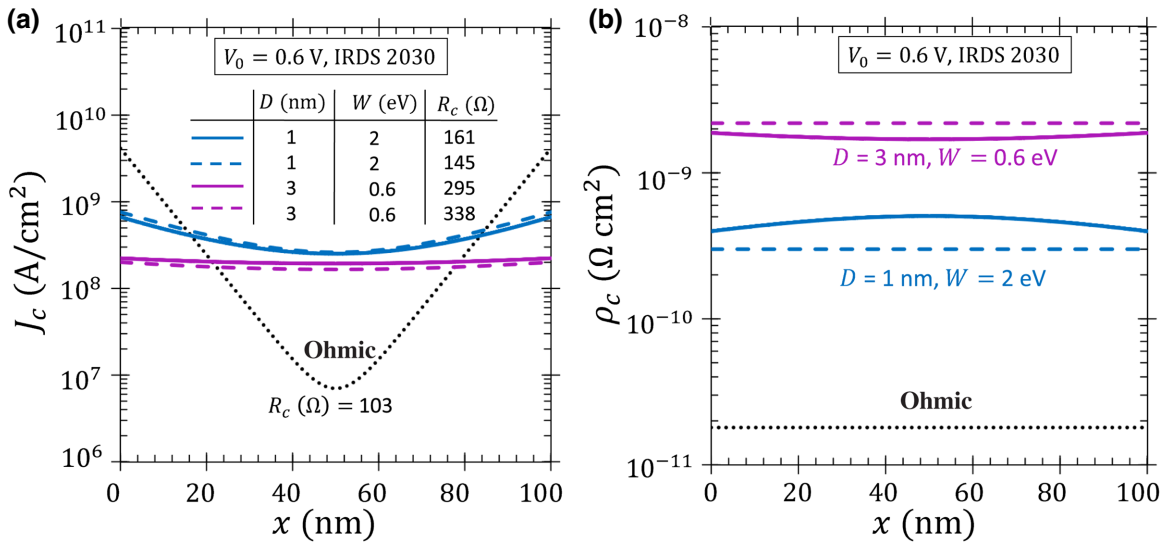


FIG. 6. Tunneling-type electrical contacts. (a) Contact-current density,  $J_c(x)$ , and (b) specific contact resistivity,  $\rho_c(x)$ , along contact length for Cartesian tunneling contacts. Solid lines are for self-consistent numerical calculations using Eqs. (1) and (2), and  $M$ - $I$ - $M$  quantum-tunneling formulations [51,69], for different values of gap distance  $D$  and work function of contact members  $W$ . Sheet resistance of both contact members is assumed to be  $R_{sh1} = R_{sh2} = 18 \Omega/\square$ . Dashed lines are calculated analytically with constant  $\rho_c$  using  $V_g = V_0$  in the 1D  $M$ - $I$ - $M$  tunneling model. Black dotted lines are for an ohmic contact with  $\rho_c = 1.8 \times 10^{-11} \Omega \text{ cm}^2$ , analytically calculated from TLM equations.  $R_c$  is the total contact resistance.

contact members  $W$ . Dashed lines are for analytical calculations [see Eq. (8) of Ref. [14]] of tunneling contacts with constant  $\rho_c$  obtained using  $V_g = V_0$  in the 1D  $M$ - $I$ - $M$  tunneling model. Sheet resistance of both contact members is assumed to be  $R_{sh1} = R_{sh2} = 18 \Omega/\square$ . We solve two cases: (i) for  $D = 1 \text{ nm}$  and  $W_1 = W_2 = 2 \text{ eV}$ , and (ii) for

$D = 3 \text{ nm}$  and  $W_1 = W_2 = 0.6 \text{ eV}$ . The interfacial layer is assumed to be vacuum (relative permittivity  $\epsilon_r = 1.0$  and electron affinity  $X = 0 \text{ eV}$ ). Black dotted lines are for an ohmic contact, calculated from Eq. (8) of Ref. [14], with specific contact resistivity  $\rho_c = 1.8 \times 10^{-11} \Omega \text{ cm}^2$ , and sheet resistance ratio  $R_{sh1}/R_{sh2} = 1$ . We use  $0.6 \text{ V}$  as the

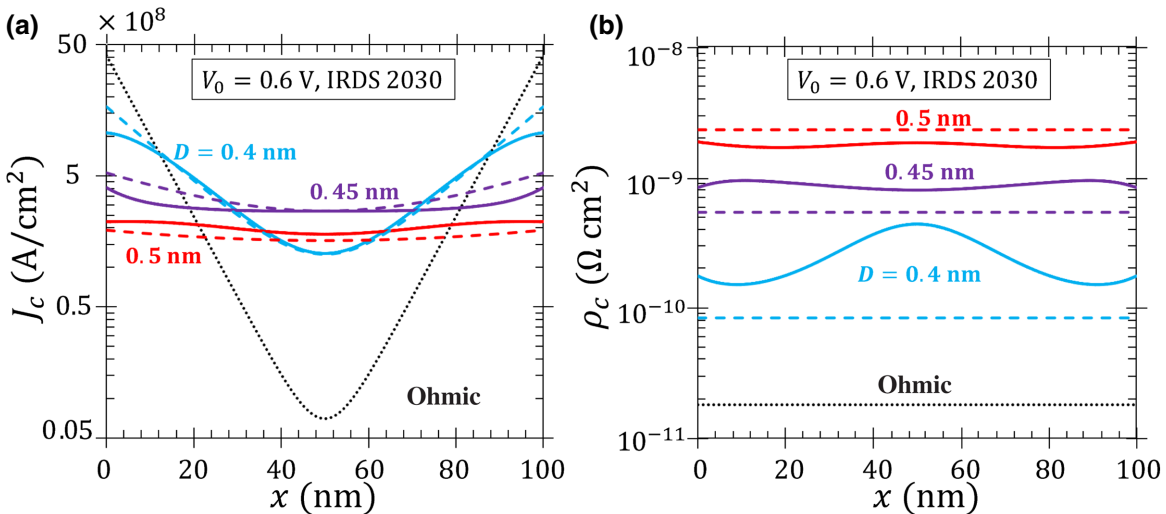


FIG. 7. Tunneling-type electrical contacts. (a) Contact-current density,  $J_c(x)$ , and (b) specific contact resistivity,  $\rho_c(x)$ , along contact length for Cartesian Cu-vacuum-Cu tunneling contacts. Solid lines are for self-consistent numerical calculations using Eqs. (1) and (2), and  $M$ - $I$ - $M$  quantum-tunneling formulations [51,69], for different values of gap distance  $D$ . Dashed lines are calculated analytically with constant  $\rho_c$  using  $V_g = V_0$  in the 1D  $M$ - $I$ - $M$  tunneling model. Black dotted lines are for an ohmic contact with  $\rho_c = 1.8 \times 10^{-11} \Omega \text{ cm}^2$ , analytically calculated from TLM equations.

input voltage, which is the required industry standard, according to the IRDS [70] for the year 2030. Additionally, we hope that this article can spur testing of the concept in the near term at 3 nm, as this will allow further development of the technology as additional manufacturing capability described in the IRDS comes online.

It is clear that the interfacial current is much more evenly distributed for contacts with a tunneling layer. Current crowding decreases significantly when the gap distance between two contact members is increased. The specific contact resistivity,  $\rho_c(x)$ , along the contact length, plotted in Fig. 6(b), is about, at most, 2 orders of magnitude higher for tunneling contacts for the two cases considered. However, the total contact resistance, shown in the table in Fig. 6(a), is still within the same order as the ohmic contact. This is because the total current in the circuit [i.e., area under the curves in Fig. 6(a)] does not decrease significantly.

Similar calculations are done for Cu-vacuum-Cu contacts in Fig. 7 with a smaller gap distance (subnanometer). The work function of Cu thin films is  $W_1 = W_2 = 4.56$  eV [71]. For these calculations, the thicknesses of both Cu contact members are 10 nm, with a resistivity of  $18 \mu\Omega \text{ cm}$  [71], which gives a sheet resistance of  $R_{\text{sh}1} = R_{\text{sh}2} = 18 \Omega/\square$ . The contact length,  $L$ , is 100 nm, and the width,  $w$ , is 10 nm. The interfacial layer is assumed to be vacuum (relative permittivity  $\epsilon_r = 1.0$  and electron affinity  $X = 0$  eV).

Figure 7 shows similar trends to those in Fig. 6. Current crowding decreases significantly when  $D$  increases. Although  $\rho_c(x)$  [Fig. 7(b)] is orders of magnitude higher

for tunneling contacts, the total contact resistance, plotted in Fig. 8(a) (cross symbols), is still within the same order as that of the ohmic contact. Therefore, compared with a perfect ohmic contact with very small  $\rho_c(x)$ , tunneling-type contacts with an ultrathin insulator layer may help to achieve better contact-current distribution and thermal management. Notably, if the gap distance is increased for contacting members with a high work function, then the junction will become highly resistive and the total current transport will be reduced severely.

Figure 8 shows the tunneling contact resistance as functions of input voltage  $V_0$  and contact length  $L$ . For low voltages, the difference between the contact resistance for the ohmic contact and the corresponding tunneling contact is prominent. However, as the voltage increases, the difference becomes smaller, which is caused by the strong increase of the tunneling current in the  $M-I-M$  towards the space-charge-limited regime [51,69]. As shown in Fig. 8(b), as the contact length increases, the increase in the total contact resistance due to the tunneling layer becomes smaller. Thus, our proposed method for reducing current crowding with a tunneling layer would become more effective for longer electrical contacts.

#### IV. PROPOSAL FOR A PROOF-OF-PRINCIPLE EXPERIMENT

In formulating our approach, we try to maintain a connection to the art of the possible in manufacturing. As noted above, enhanced performance via current spreading in the tunneling-type contacts with acceptable contact

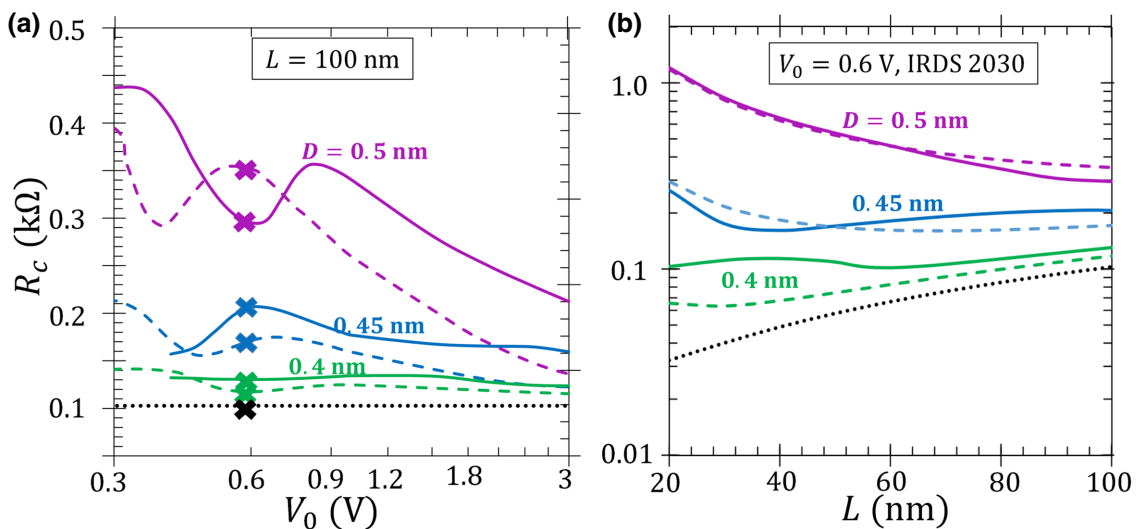


FIG. 8. Contact resistance as a function of (a) input voltage  $V_0$  and (b) contact length  $L$  for Cartesian Cu-vacuum-Cu tunneling contacts. Solid lines are self-consistent numerical calculations using Eqs. (1) and (2), and  $M-I-M$  quantum-tunneling formulations [51,69], for different values of gap distance  $D$ . Dashed lines are calculated analytically with constant  $\rho_c$  using  $V_g = V_0$  in the 1D  $M-I-M$  tunneling model. Black dotted lines are for an ohmic contact with  $\rho_c = 1.8 \times 10^{-11} \Omega \text{ cm}^2$ , which is analytically calculated from the TLM equations. Crosses in (a) are for the four cases shown in Fig. 7.



resistance can be achieved for structures that are sufficiently thin, typically less than 1 nm. Industry roadmaps suggest that this is possible in time frame of the 2030s through plasma-etching techniques. Additionally, we note that atomic layer deposition (ALD), while far less common than plasma processing, can produce atomically thin structures presently. We understand the challenge in determining the cost-benefit analysis for the performance and lifetime of an advanced contact at the current point in time, where it is just outside the art of the possible (etching) or requires a process that is exotic (ALD). We anticipate that, for certain applications that require high currents and ruggedized physical performance, as might be needed in national security and defense applications, there may be value in developing and deploying ALD to make these kinds of contacts today. More likely, however, it will be necessary to first experimentally verify and validate these engineered contacts and develop uncertainty quantification of the performance of the contact in a variety of applications, to better assess this cost-benefit trade-off. To that end, we propose a proof-of-principle (POP) experiment here based on existing 3-nm plasma-etching manufacturing. It is not our intention to suggest that this thick contact will be appropriate for fielding, but rather will allow the benefits and drawback of the experimental performance of this technology to be accurately assessed. In our reading of the literature, we note that, while our POP experiment might have twice the contact resistance of a standard ohmic contact, it is still low enough to provide experimental data for characterization, especially when compared with the contact resistance seen in thin films and two-dimensional material interfaces. Specialty fabrication facilities, such as the Metal Oxide Semiconductor Implementation Service (MOSIS) [83], would allow for the designs in this paper to be tested in application-specific integrated circuits (ASICs) with relatively modest costs. Furthermore, the recent announcement of 2-nm chip technology by IBM [84] will make the 10 s of nm variation along a contact interface feasible, where our proposed scheme can be implemented.

## V. SUMMARY

We propose methods to effectively control current distribution and contact resistance in nanoscale electrical contacts. We use the two-dimensional TLM [12,14] for ohmic contacts, the TLM coupled with the thermionic injection model [40,48] for Schottky contacts, and the quantum self-consistent model [51,69] for tunneling-type contacts. Our study shows that severe current crowding in highly conductive electrical contacts can be effectively reduced by spatially varying the contact-layer properties and geometry or by introducing a thin (nanometer or subnanometer scale) insulator layer between the contacting members. This theoretical study also provides insights for strategic current

steering and redistribution at the contact interface, which can aid in better thermal management of the overall circuit. Local heating-induced effects, such as thermal hot spots [19] and aggravation of electromigration [23], can be mitigated by manipulating the specific contact resistivity along the contact length.

It is worthwhile to note that the effects of the transverse dimension, possible charge trapping inside the contact layer, reactive elements, and their effects on the time-dependent dynamics are ignored in the present study. Moreover, the transmission-line model [14] cannot fully capture current crowding and fringing fields near the contact corners [13,18,52]. In future, field-solution methods [13,52,85] may be used for a more accurate evaluation of these effects, as well as the impact of the finite thickness of the contact members and the interfacial layer.

Finally, we argue for a near-term demonstration of these engineered contacts in ASIC chips with relatively thick gaps ( $\sim 3$  nm). This experimental testing can be achieved in the near term, without waiting for advances in manufacturing that would allow the full benefits of the tunneling contact to be realized.

## ACKNOWLEDGMENTS

The work is supported by the Air Force Office of Scientific Research (AFOSR) YIP Grant No. FA9550-18-1-0061.

## APPENDIX: CONTACT ENGINEERING WITH STEP VARIATIONS IN INTERFACIAL LAYER

In Fig. 3 of the main text, we show that severe current crowding in highly conductive ohmic contacts with similar contact members can be eliminated by varying the specific contact resistivity,  $\rho_c$ , parabolically. Similarly, in Fig. 5, we show that the nonuniformity of the current distribution at a 2D semiconductor-3D metal interface can be reduced if the SBH is varied as a quadratic function along the contact length.

Here, we would like to point out that the specific contact resistivity or the SBH needs not necessarily be a smooth parabola, a quadratic function, or some other complex function. The strong current-crowding effect along the contact interface can be mitigated with simpler variations of  $\rho_c$  along  $x$ , which may be more easily implemented in practice. We provide additional calculations that show current crowding can also be reduced by varying  $\rho_c$  as a simple step function along  $x$ . The recent announcement of 2-nm chip technology by IBM [84] will make the 10 s of nm variation along a contact interface feasible, where our proposed scheme can be implemented.

Since the current crowds most at the two edges of planar parallel electrical contacts with similar contact members, we make  $\rho_c$  at the two edges larger than that of the center in Figs. 9(a) and 9(c). This can be done by either

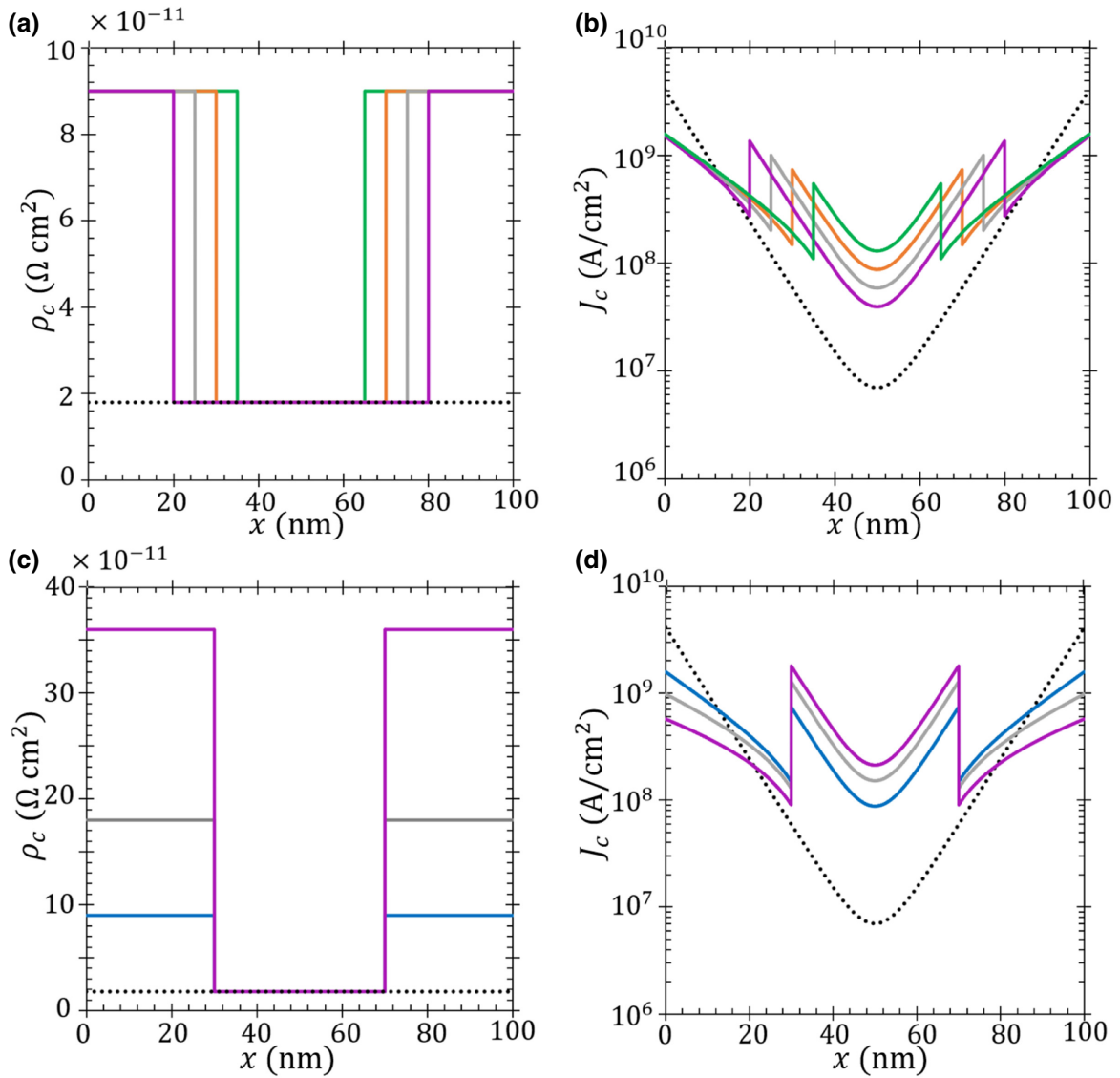


FIG. 9. Engineered ohmic contact in Cartesian geometry. (a),(c) Step-varying specific contact resistivity,  $\rho_c(x)$ ; (b),(d) corresponding contact-current density,  $J_c(x)$ , along contact length. Input voltage  $V_0 = 0.6$  V is the required industry standard, according to the IRDS for the year 2030 [70]. Thicknesses of both Cu contact members are 10 nm, with a resistivity of  $18 \mu\Omega \text{ cm}$ , which gives  $R_{\text{sh1}} = R_{\text{sh2}} = 18 \Omega/\square$ . Contact length,  $L$ , is 100 nm, and width (transverse dimension),  $w$ , of contact members is 10 nm.

varying the geometry of the contact members (i.e., making the interface layer thicker at the edges) or introducing oxides or contaminants at the edges. The corresponding current-density profiles are shown in Figs. 9(b) and 9(d), respectively. The black dotted lines are for nonengineered contacts, with uniform  $\rho_c$ . We see that current crowding at the two edges is reduced significantly (note the  $\log_{10}$  scale used) for the engineered contacts.

For the 2D semiconductor-3D metal interface, the current crowds at the leading edge because of the resistivity mismatch between the two contact members. For  $\text{MoS}_2/\text{Au}$  contacts in Fig. 10(a), we vary the SBH along  $x$  as a step function, increasing it at the leading

edge and decreasing it elsewhere. Figure 10(b) shows the corresponding contact-current densities  $J_c$ . The black dotted lines are for a uniform SBH. We see that, although the profiles are not smooth nor uniform, current crowding at the leading edge ( $x = 0$ ) is reduced significantly. The total contact resistance,  $R_c$ , is almost unchanged.

Notably, the sharp transitions of the contact-current density in Figs. 9(b), 9(d), and 10(b) are due to the assumed abrupt changes in the specific contact resistivity at those regions. In practical fabrication, the step functions typically gradually vary, which will smooth the sharp peaks in  $J_c$ .

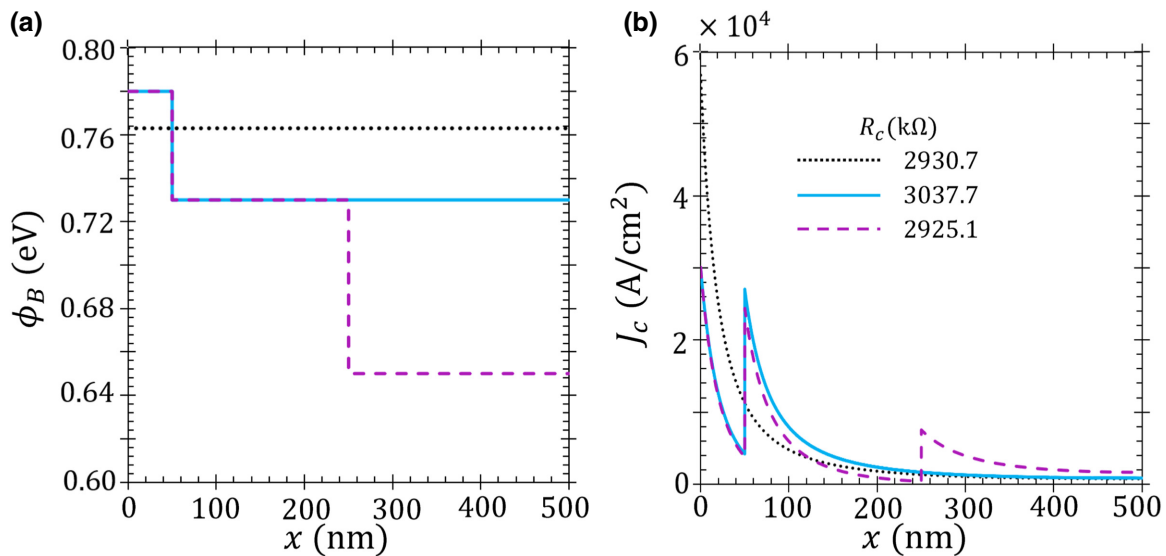


FIG. 10. Engineered Schottky contacts in Cartesian geometry. (a) Step-varying Schottky barrier height,  $\phi_B(x)$ ; (b) corresponding contact-current density,  $J_c(x)$ , along contact length for MoS<sub>2</sub>/Au contacts. Corresponding contact resistances are mentioned in (b). Black dotted lines are for MoS<sub>2</sub>/Au contacts with uniform  $\phi_B = 0.763$  eV.  $\epsilon_F = 0.077$  eV,  $\tau = 0.1$  ps, and  $V_0 = 0.65$  V. Here,  $R_{sh1}(\text{MoS}_2) = 59171.6 \Omega/\square$ ,  $R_{sh2}(\text{Au}) = 2.2 \Omega/\square$ ,  $L = 500$  nm,  $w = 10$  nm, and  $T = 300$  K.

- [1] L.-M. Peng, A new stage for flexible nanotube devices, *Nat. Electron.* **1**, 158 (2018).
- [2] P. Zhang, S. Banerjee, and J. Luginsland, Tunneling electrical contacts, U.S. Patent 10,755,975 B2 (25 August 2020).
- [3] C. S. Lau, J. Y. Chee, Y. S. Ang, S. W. Tong, L. Cao, Z.-E. Ooi, T. Wang, L. K. Ang, Y. Wang, M. Chhowalla, and K. E. J. Goh, Quantum transport in two-dimensional WS<sub>2</sub> with high-efficiency carrier injection through indium alloy contacts, *ACS Nano* **14**, 13700 (2020).
- [4] A. Allain, J. Kang, K. Banerjee, and A. Kis, Electrical contacts to two-dimensional semiconductors, *Nat. Mater.* **14**, 1195 (2015).
- [5] J. Tang, Q. Cao, G. Tulevski, K. A. Jenkins, L. Nela, D. B. Farmer, and S.-J. Han, Flexible CMOS integrated circuits based on carbon nanotubes with sub-10 ns stage delays, *Nat. Electron.* **1**, 191 (2018).
- [6] X. He, W. Gao, L. Xie, B. Li, Q. Zhang, S. Lei, J. M. Robinson, E. H. Házroz, S. K. Doorn, W. Wang, R. Vajtai, P. M. Ajayan, W. W. Adams, R. H. Hauge, and J. Kono, Wafer-scale monodomain films of spontaneously aligned single-walled carbon nanotubes, *Nat. Nanotechnol.* **11**, 633 (2016).
- [7] J. Zaumseil, Single-walled carbon nanotube networks for flexible and printed electronics, *Semicond. Sci. Technol.* **30**, 074001 (2015).
- [8] K. L. Grosse, M.-H. Bae, F. Lian, E. Pop, and W. P. King, Nanoscale Joule heating, Peltier cooling and current crowding at graphene-metal contacts, *Nat. Nanotechnol.* **6**, 287 (2011).
- [9] D. J. Oliver, J. Maassen, M. E. Ouali, W. Paul, T. Hagedorn, Y. Miyahara, Y. Qi, H. Guo, and P. Grütter, Conductivity of an atomically defined metallic interface, *Proc. Natl. Acad. Sci.* **109**, 19097 (2012).
- [10] K. Croes, Y. Li, M. Lofrano, C. J. Wilson, and Z. Tókei, in *2013 IEEE Int. Reliab. Phys. Symp. IRPS 2C.3.1* (2013).
- [11] H. Murrmann and D. Widmann, Current crowding on metal contacts to planar devices, *IEEE Trans. Electron Devices* **16**, 1022 (1969).
- [12] S. Banerjee, P. Y. Wong, and P. Zhang, Contact resistance and current crowding in tunneling type circular nano-contacts, *J. Phys. D: Appl. Phys.* **53**, 355301 (2020).
- [13] P. Zhang, Y. Y. Lau, and R. M. Gilgenbach, Analysis of current crowding in thin film contacts from exact field solution, *J. Phys. D: Appl. Phys.* **48**, 475501 (2015).
- [14] S. Banerjee, J. Luginsland, and P. Zhang, A two dimensional tunneling resistance transmission line model for nanoscale parallel electrical contacts, *Sci. Rep.* **9**, 14484 (2019).
- [15] D. K. Schroder, *Semiconductor Material and Device Characterization*, 2nd ed. (Wiley-Blackwell, New York, 1998).
- [16] P. Yang, S. Banerjee, W. Kuang, Y. Ding, Q. Ma, and P. Zhang, Current crowding and spreading resistance of electrical contacts with irregular contact edges, *J. Phys. D: Appl. Phys.* **53**, 485303 (2020).
- [17] H. H. Berger, Contact resistance and contact resistivity, *J. Electrochem. Soc.* **119**, 507 (1972).
- [18] Q. Wang, X. Tao, L. Yang, and Y. Gu, Current crowding in two-dimensional black-phosphorus field-effect transistors, *Appl. Phys. Lett.* **108**, 103109 (2016).
- [19] X. Zhao, M. R. Scheuermann, and S. K. Lim, Analysis and modeling of DC current crowding for TSV-based 3-D connections and power integrity, *IEEE Trans. Compon. Packag. Manuf. Technol.* **4**, 123 (2014).

- [20] A. Bar-Cohen and P. Wang, Thermal management of On-chip hot spot, *J. Heat Transf.* **134**, 051017 (2012).
- [21] S. W. Liang, Y. W. Chang, and C. Chen, Relieving hot-spot temperature and current crowding effects during electromigration in solder bumps by using Cu columns, *J. Electron. Mater.* **36**, 1348 (2007).
- [22] A. V. Zinovchuk, O. Yu. Malyutenko, V. K. Malyutenko, A. D. Podoltsev, and A. A. Vilisov, The effect of current crowding on the heat and light pattern in high-power AlGaAs light emitting diodes, *J. Appl. Phys.* **104**, 033115 (2008).
- [23] J. S. Huang, E. C. C. Yeh, Z. B. Zhang, and K. N. Tu, The effect of contact resistance on current crowding and electromigration in ULSI multi-level interconnects, *Mater. Chem. Phys.* **77**, 377 (2003).
- [24] T. L. Shao, Y. H. Chen, S. H. Chiu, and C. Chen, Electromigration failure mechanisms for SnAg3.5 solder bumps on Ti/Cr-Cu/Cu Ni(P)/Au metallization pads, *J. Appl. Phys.* **96**, 4518 (2004).
- [25] W. J. Choi, E. C. C. Yeh, and K. N. Tu, Mean-time-to-failure study of flip chip solder joints on Cu/Ni(V)/Al thin-film under-bump-metallization, *J. Appl. Phys.* **94**, 5665 (2003).
- [26] Y. Park, J. Joh, J. Chung, and S. Krishnan, in *2019 IEEE Int. Reliab. Phys. Symp. IRPS* (2019), pp. 1–6.
- [27] I. L. Markov, Limits on fundamental limits to computation, *Nature* **512**, 147 (2014).
- [28] M. Rokni and Y. Levinson, in *Proc. Int. Workshop Phys. Comput. Model. Devices Based Low-Dimens. Struct.* **14** (1995).
- [29] S. K. Thangaraju and K. M. Munisamy, Electrical and Joule heating relationship investigation using Finite Element Method, *IOP Conf. Ser. Mater. Sci. Eng.* **88**, 012036 (2015).
- [30] P. Zhang, S. B. Fairchild, T. C. Back, and Y. Luo, Field emission from carbon nanotube fibers in varying anode-cathode gap with the consideration of contact resistance, *AIP Advances* **7**, 125203 (2017).
- [31] E. Pop, The role of electrical and thermal contact resistance for joule breakdown of single-wall carbon nanotubes, *Nanotechnology* **19**, 295202 (2008).
- [32] F. Antoulakis, D. Chernin, P. Zhang, and Y. Y. Lau, Effects of temperature dependence of electrical and thermal conductivities on the joule heating of a one dimensional conductor, *J. Appl. Phys.* **120**, 135105 (2016).
- [33] Chien-Neng Liao and Kuan-Chia Chen, Current crowding effect on thermal characteristics of Ni/doped-Si contacts, *IEEE Electron Device Lett.* **24**, 637 (2003).
- [34] I. Ratković, N. Bežanić, O. S. Ünsal, A. Cristal, and V. Milutinović, in *Adv. Comput.*, edited by A. R. Hurson (Elsevier, 2015).
- [35] M. Pedram, Power minimization in IC design: Principles and applications, *ACM Trans. Des. Autom. Electron. Syst.* **1**, 3 (1996).
- [36] E. P. Vandamme and L. K. J. Vandamme, Current crowding and its effect on 1/f noise and third harmonic distortion – a case study for quality assessment of resistors, *Microelectron. Reliab.* **40**, 1847 (2000).
- [37] H. Yuan, G. Cheng, S. Yu, A. R. Hight Walker, C. A. Richter, M. Pan, and Q. Li, Field effects of current crowding in metal-MoS<sub>2</sub> contacts, *Appl. Phys. Lett.* **108**, 103505 (2016).
- [38] P. Karnatak, T. P. Sai, S. Goswami, S. Ghatak, S. Kaushal, and A. Ghosh, Current crowding mediated large contact noise in graphene field-effect transistors, *Nat. Commun.* **7**, 13703 (2016).
- [39] K. Nagashio, T. Nishimura, K. Kita, and A. Toriumi, Contact resistivity and current flow path at metal/graphene contact, *Appl. Phys. Lett.* **97**, 143514 (2010).
- [40] S. Banerjee, L. Cao, Y. S. Ang, L. K. Ang, and P. Zhang, Reducing Contact Resistance in Two-Dimensional-Material-Based Electrical Contacts by Roughness Engineering, *Phys. Rev. Appl.* **13**, 064021 (2020).
- [41] C.-K. Wang, T.-H. Chiang, Y.-Z. Chiou, and S.-P. Chang, Reducing the current crowding effect on nitride-based light-emitting diodes using modulated P-extension electrode thickness, *Jpn. J. Appl. Phys.* **52**, 01AG05 (2013).
- [42] G. Kim, J. H. Kim, E. Park, and B.-G. Park, Reduction of current crowding in InGaN-based blue light-emitting diodes by modifying metal contact geometry, *J. Semicond. Technol. Sci.* **14**, 588 (2014).
- [43] N. Shamir and D. Ritter, Reducing the current crowding effect in bipolar transistors by tunnel diode emitter design, *Solid-State Electron.* **47**, 127 (2003).
- [44] S.-S. Chee, D. Seo, H. Kim, H. Jang, S. Lee, S. P. Moon, K. H. Lee, S. W. Kim, H. Choi, and M.-H. Ham, Lowering the Schottky barrier height by graphene/Ag electrodes for high-mobility MoS<sub>2</sub> field-effect transistors, *Adv. Mater.* **31**, 1804422 (2019).
- [45] Y. Zhang, M. Sun, D. Piedra, J. Hennig, A. Dadgar, and T. Palacios, Reduction of on-resistance and current crowding in quasi-vertical GaN power diodes, *Appl. Phys. Lett.* **111**, 163506 (2017).
- [46] F. Torricelli, L. Colalongo, D. Raiteri, Z. M. Kovács-Vajna, and E. Cantatore, Ultra-high gain diffusion-driven organic transistor, *Nat. Commun.* **7**, 10550 (2016).
- [47] P. Zhang, Y. Y. Lau, and R. S. Timsit, On the spreading resistance of thin-film contacts, *IEEE Trans. Electron Devices* **59**, 1936 (2012).
- [48] Y. S. Ang, H. Y. Yang, and L. K. Ang, Universal Scaling Laws in Schottky Heterostructures Based on Two-Dimensional Materials, *Phys. Rev. Lett.* **121**, 056802 (2018).
- [49] J. G. Simmons, Generalized formula for the electric tunnel effect between similar electrodes separated by a thin insulating film, *J. Appl. Phys.* **34**, 1793 (1963).
- [50] J. G. Simmons, Electric tunnel effect between dissimilar electrodes separated by a thin insulating film, *J. Appl. Phys.* **34**, 2581 (1963).
- [51] P. Zhang, Scaling for quantum tunneling current in nano- and subnano-scale plasmonic junctions, *Sci. Rep.* **5**, 9826 (2015).
- [52] P. Zhang and Y. Y. Lau, An exact field solution of contact resistance and comparison with the transmission line model, *Appl. Phys. Lett.* **104**, 204102 (2014).
- [53] N. Chiodarelli, S. Masahito, Y. Kashiwagi, Y. Li, K. Arstila, O. Richard, D. J. Cott, M. Heyns, S. De Gendt, G. Groeseneken, and P. M. Vereecken, Measuring the electrical resistivity and contact resistance of vertical



- carbon nanotube bundles for application as interconnects, *Nanotechnology* **22**, 085302 (2011).
- [54] D. K. Schroder and D. L. Meier, Solar cell contact resistance—A review, *IEEE Trans. Electron Devices* **31**, 637 (1984).
- [55] K. N. Tu, Y. Liu, and M. Li, Effect of Joule heating and current crowding on electromigration in mobile technology, *Appl. Phys. Rev.* **4**, 011101 (2017).
- [56] A. D. Franklin, D. B. Farmer, and W. Haensch, Defining and overcoming the contact resistance challenge in scaled carbon nanotube transistors, *ACS Nano* **8**, 7333 (2014).
- [57] P. Zhang, A. Valfells, L. K. Ang, J. W. Luginsland, and Y. Y. Lau, 100 years of the physics of diodes, *Appl. Phys. Rev.* **4**, 011304 (2017).
- [58] P. Zhang and Y. Y. Lau, Ultrafast and nanoscale diodes, *J. Plasma Phys.* **82**, 595820505 (2016).
- [59] J. Lin, P. Y. Wong, P. Yang, Y. Y. Lau, W. Tang, and P. Zhang, Electric field distribution and current emission in a miniaturized geometrical diode, *J. Appl. Phys.* **121**, 244301 (2017).
- [60] P. Zhang and D. M. H. Hung, An analytical model for ballistic diode based on asymmetric geometry, *J. Appl. Phys.* **115**, 204908 (2014).
- [61] P. Zhang, Y. S. Ang, A. L. Garner, A. Valfells, J. W. Luginsland, and L. K. Ang, Space-charge limited current in nanodiodes: Ballistic, collisional and dynamical effects, *J. Appl. Phys.* **129**, 100902 (2021).
- [62] P. Zhang, J. Park, S. B. Fairchild, N. P. Lockwood, Y. Y. Lau, J. Ferguson, and T. Back, Temperature comparison of looped and vertical carbon nanotube fibers during field emission, *Appl. Sci.* **8**, 1175 (2018).
- [63] S. B. Fairchild, P. Zhang, J. Park, T. C. Back, D. Marincel, Z. Huang, and M. Pasquali, Carbon nanotube fiber field emission array cathodes, *IEEE Trans. Plasma Sci.* **47**, 2032 (2019).
- [64] X. Xiong, Y. Zhou, Y. Luo, X. Li, M. Bosman, L. K. Ang, P. Zhang, and L. Wu, Plasmon-enhanced resonant photoemission using atomically-thick dielectric coatings, *ACS Nano* **14**, 8806 (2020).
- [65] Y. Zhou and P. Zhang, Theory of field emission from dielectric coated surfaces, *Phys. Rev. Res.* **2**, 043439 (2020).
- [66] J. M. Connelly, W. W. Tang, J. R. Harris, and K. L. Jensen, Demonstration of 3-D-printed field-emission cathodes, *IEEE Trans. Plasma Sci.* **47**, 4292 (2019).
- [67] W. Tang, D. Shiffler, K. Golby, M. LaCour, and T. Knowles, Field enhancement for fiber emitters in linear and rectangular arrays, *J. Vac. Sci. Technol. B Nanotechnol. Microelectron. Mater. Process. Meas. Phenom.* **32**, 052202 (2014).
- [68] M. W. Swift and Y. Qi, First-Principles Prediction of Potentials and Space-Charge Layers in All-Solid-State Batteries, *Phys. Rev. Lett.* **122**, 167701 (2019).
- [69] S. Banerjee and P. Zhang, A generalized self-consistent model for quantum tunneling current in dissimilar metal-insulator-metal junction, *AIP Adv.* **9**, 085302 (2019).
- [70] International Roadmap for Devices and Systems (IRDS™). (2017). <https://irds.ieee.org/editions/2017> (accessed May 05, 2020).
- [71] E. Schmiedl, P. Wissmann, and H.-U. Finzel, The electrical resistivity of ultra-thin copper films, *Z. Für Naturforschung A* **63**, 739 (2014).
- [72] J. G. J. Chern and W. G. Oldham, Determining specific contact resistivity from contact end resistance measurements, *IEEE Electron Device Lett.* **5**, 178 (1984).
- [73] K. K. Ng and R. Liu, On the calculation of specific contact resistivity on, *IEEE Trans. Electron Devices* **37**, 1535 (1990).
- [74] S. Gupta, P. Paramahans Manik, R. Kesh Mishra, A. Nainani, M. C. Abraham, and S. Lodha, Contact resistivity reduction through interfacial layer doping in metal-interfacial layer-semiconductor contacts, *J. Appl. Phys.* **113**, 234505 (2013).
- [75] F. A. Chaves, D. Jiménez, A. W. Cummings, and S. Roche, Physical model of the contact resistivity of metal-graphene junctions, *J. Appl. Phys.* **115**, 164513 (2014).
- [76] G. Shine and K. C. Saraswat, in *2013 Int. Conf. Simul. Semicond. Process. Devices SISPAD* 69 (2013).
- [77] H. Zhong, R. Quhe, Y. Wang, Z. Ni, M. Ye, Z. Song, Y. Pan, J. Yang, L. Yang, M. Lei, J. Shi, and J. Lu, Interfacial properties of monolayer and bilayer MoS<sub>2</sub> contacts with metals: Beyond the energy band calculations, *Sci. Rep.* **6**, 21786 (2016).
- [78] D. Sinha and J. U. Lee, Ideal graphene/silicon Schottky junction diodes, *Nano Lett.* **14**, 4660 (2014).
- [79] M. Javadi, A. Noroozi, and Y. Abdi, Kinetics of Charge Carriers Across a Graphene-Silicon Schottky Junction, *Phys. Rev. Appl.* **14**, 064048 (2020).
- [80] J. P. Perdew and Y. Wang, Accurate and simple analytic representation of the electron-gas correlation energy, *Phys. Rev. B* **45**, 13244 (1992).
- [81] M. Lapedus and E. Sperling, Making chips At 3 nm and beyond, *Semicond. Eng.* (2020). <https://semiengineering.com/making-chips-at-3nm-and-beyond/> (accessed Feb. 09, 2021).
- [82] A. Frumusanu, TSMC Details 3 nm Process Technology: Full Node Scaling for 2H22 Volume Production. <https://www.anandtech.com/show/16024/tsmc-details-3-nm-process-technology-details-full-node-scaling-for-2h22> (accessed Feb. 26, 2021).
- [83] MOSIS, (<https://www.mosis.com/>) (accessed Mar. 16, 2021).
- [84] IBM Unveils World's First 2 Nanometer Chip Technology, Opening a New Frontier for Semiconductors, IBM News Room, Albany, N.Y. (2021). <https://newsroom.ibm.com/2021-05-06-IBM-Unveils-Worlds-First-2-Nanometer-Chip-Technology,-Opening-a-New-Frontier-for-Semiconductors> (accessed May 28, 2021).
- [85] P. Zhang, D. M. H. Hung, and Y. Y. Lau, Current flow in a 3-terminal thin film contact with dissimilar materials and general geometric aspect ratios, *J. Phys. D: Appl. Phys.* **46**, 065502 (2013).